Acta Materialia 316 (2026) 122498

Contents lists available at ScienceDirect

Acta Materialia

journal homepage: www.elsevier.com/locate/actamat

Full length article

Influence of sample size, strain rate and temperature on deformation of an Fe-2.4 wt.% Si Bi-crystal and its paired single crystals

Chunhua Tian [a,*], Hexin Wang [a], Pei-Ling Sun [a], Martina Freund [a], Marcus Hans [b], Maral Sarebanzadeh [c], Zhuocheng Xie [a], Gaurav Mohanty [d], Jakob Schwiedrzik [e], Sandra Korte-Kerzel [a]

[a] Institute for Physical Metallurgy and Materials Physics, RWTH Aachen University, 52074, Aachen, Germany
[b] Materials Chemistry, RWTH Aachen University, 52074, Aachen, Germany
[c] Institute for Applied Materials, KIT, Karlsruhe, 76131, Germany
[d] Materials Science and Environmental Engineering, Tampere University, 33014, Tampere, Finland
[e] Empa Swiss Federal Laboratory for Material Science and Technology, Laboratory of Mechanics of Materials and Nanostructures, Feuerwerkerstrasse 39, 3603, Thun, Switzerland

ARTICLE INFO

Keywords:
Grain boundary
Slip transmission
Microcompression
Cryogenic temperature
Strain rate
Sample size

ABSTRACT

Grain boundaries play an important role in determining mechanical properties of materials. To investigate the behavior of a single grain boundary, micropillar compression on bi-crystals has been widely applied, which however, mainly focuses on face-centered cubic metals. In this work, we investigate the influence of micropillar size, strain rate and temperature on deformation behavior of an Fe-2.4 wt.% Si bi-crystal with a high angle grain boundary and its paired single crystals. Tests were carried out at room temperature and -80 °C, nominal micropillar sizes were 1 μm, 2 μm and 4 μm, while strain rates were 0.001 s^{-1}, 0.01 s^{-1} and 0.1 s^{-1}. Slip trace analysis reveals slip transmission across the grain boundary in bi-crystalline pillars. The transmitted slip systems can be different from those activated in single crystals depending on orientation. The identified transmission pair has a high transmission factor and is insensitive to strain rate and temperature, but dependent on pillar size. In contrast, the difference in yield strength between bi-crystals and single crystals is more closely related to testing parameters. For single crystals, smaller pillars can activate slip systems with a lower Schmid factor and slip traces become wavy due to cross-slip at a sub-ambient temperature.

1. Introduction

Grain boundaries are ubiquitous microstructural features in crystalline materials and play a critical role in determining mechanical properties. In most cases, they act as obstacles for dislocation movement [1,2], which leads to the well-known grain refinement strengthening described by the Hall-Petch equation [3]. However, grain boundaries are not always barriers against plasticity, but can also act as dislocation sinks [4], sources [5] or allow transmission of dislocations [6]. Hence, to better understand the role of grain boundaries, attention has been directed to investigate a specific grain boundary by a variety of micro-mechanical tests [7–9], in particular bi-crystals by micropillar compression [4,10,11] in order to circumvent the growth of macroscopic single and bi-crystals [12]. These studies reported that the role of grain boundaries in mechanical deformation of bi-crystal micropillars depends on different factors. While a large angle grain boundary in copper leads to dislocation pile-up strengthening, a coherent twin boundary is transparent to dislocation motion and barely increases the bi-crystal strength [13]. In addition, micropillar size also matters. For bi-crystalline nickel pillars, the yield strength can be either lower (5 μm) or higher (1 μm) than that of single crystalline counterparts [10]. Significant strain hardening is observed in 5 μm bi-crystalline pillars, whereas it was reported absent in 1 μm pillars [14]. Furthermore, at a low strain rate (10^{-4} s^{-1}), the bi-crystal copper pillar with a high angle grain boundary has a comparable strength with single crystals, whereas significantly higher at a larger testing strain rate (10^{-1} s^{-1}) [15]. However, the investigations above on bi-crystals with micropillar compression predominantly focused on face-centered cubic (FCC) materials. Deformation studies of body-centered cubic (BCC) bi-crystals are extremely limited. Notable exceptions are studies in [12], which

* Corresponding author.
E-mail address: tian@imm.rwth-aachen.de (C. Tian).

https://doi.org/10.1016/j.actamat.2026.122498
Received 24 February 2026; Received in revised form 24 June 2026; Accepted 24 June 2026
Available online 25 June 2026

addresses size effects in an Fe–Si bi-crystal, and in [16], which probes slip transmission in pure tantalum bi-crystals. The role of testing parameters, including strain rate and temperature, in BCC bi-crystal deformation remains largely unexplored.

To understand and predict the deformation behavior in a BCC bi-crystal compared with FCC, the higher complexity of BCC deformation needs to be considered, since not only factors such as grain boundary type, micropillars size, and testing parameters are relevant, but also the disputed slip planes. Unlike FCC structures with defined slip systems $\{111\}\langle 110\rangle$, there are still controversial reports on slip system activation in BCC single crystals [17]. Even confined to iron and its alloys, while slip direction is defined as $\langle 111\rangle$, the observed slip planes encompass a wide range of possibilities, including $\{110\}$, $\{112\}$, $\{123\}$ and maximum resolved shear stress plane (MRSSP) [18,19]. Moreover, the slip plane activation and corresponding critical resolved shear stress (CRSS) exbibit a strong dependence on orientation [20], temperature [21], and loading type (tension/compression) [22]. The mechanical behavior of bi-crystals can be closely related to the easiness of slip transmission across grain boundaries that is determined by the geometrical configuration of activated slip systems in single crystalline halves. Such geometrical configuration can be described by a transmission factor m' as defined in Eq. 1 by Luster and Morris in 1995 [23], where ψ denotes the angle between the slip plane normals and κ between slip plane directions of the two accounted slip systems in two grains. Hence, with a large pool of possible slip planes and their sensitivity to multiple factors, slip transmission behavior can change in terms of transmission capacity and transmission pair under different conditions.

$$m' = \cos\psi \cdot \cos\kappa \tag{1}$$

In this study, we use micropillar compression experiments to investigate the deformation behavior of an Fe-2.4 wt.% Si bi-crystal with a high angle grain boundary and its adjacent single crystals. As electric steels, this type of alloy is rolled into very thin sheets to reduce eddy current losses [24] and cut or stamped into final shape. With the sheet thickness comparable to grain size and processing routes involving high speed deformation, understanding the mechanical response of individual grain boundaries and their neighboring single crystals, as well as any effects of thermal activation, become particularly important. Our focus in this work is therefore the influence of sample size, strain rate and temperature on plastic deformation in single and bi-crystals.

2. Experimental procedures

2.1. Sample and experimental preparation

The macroscopic bi-crystal was grown at 0.1 mm/min according to the vertical Bridgman–Stockbarger method, using high-purity iron alloyed with Fe65wt%Si to obtain Fe-2.4 wt.% Si [12]. The as-grown material has a low dislocation density of $\sim 9 \times 10^{12}$ m^{-2} as confirmed by electron channeling contrast imaging (ECCI) with an image provided in Fig. S1. The imaging was performed using a Zeiss Merlin field emission SEM at 30 kV, with a probe current of 4 nA and a working distance of 6 mm. The sample was slightly tilted (up to ~3°) during imaging to optimize channeling contrast. The relative dislocation density was estimated by counting visible dislocation contrasts per unit image area using ImageJ. Discs for micropillars were cut from the grown crystal by electrical discharge machining (EDM). A flat surface was achieved by a final polishing with OP-U suspension (Struers). The two single crystals adjacent to the grain boundary are denoted as G1 and G2 in this manuscript. The crystal orientation was measured by electron backscattered diffraction (EBSD) on a Mira scanning electron microscope (SEM) with an EDAX DigiView camera. The average Bunge Euler angles of G1 and G2 are $\{198°, 53°, 71°\}$ and $\{351°, 84°, 355°\}$, respectively. The two crystals have a misorientation angle of 50° around the axis $[\overline{14}\ 1\ \overline{8}]$.

In order to better visualize and describe the orientation of the two crystals, they are pinpointed in the inverse pole figure (IPF) (Fig. 1a), with G1 inside the triangle and G2 near the 001–111 boundary. The IPF is further colored into different regions according to the highest Schmid factor of the three slip plane families $\{110\}$, $\{112\}$ and $\{123\}$. For instance, in the red region, slip systems with $\{110\}$ planes have the highest Schmid factor. Further, $\{112\}$ is commonly differentiated between $\{112\}_T$ and $\{112\}_{AT}$, with the former shearing $\{112\}$ plane in the twinning sense and the latter in the anti-twinning sense. Under compression, as in this work, $\{112\}_T$ is near the 101 – 111 boundary and $\{112\}_{AT}$ near the 001 corner, and vice versa under tension [20]. Hence, G2 is located in the $\{112\}_{AT}$ region and G1 in the $\{123\}$ region.

In addition to the IPF, we further describe the two crystals in terms of their χ angle to facilitate the discussion on slip plane activation, as shown in Fig. 1b [17]. In a cubic stereogram (using G1 as an example), the χ angle denotes the angle between the MRSSP that contains the slip direction $[1\ \overline{1}\ 1]$ and the neighboring$[1\ 1\ 0]$ plane. The MRSSP is determined by the intersection of the great circle passing through $[1\ \overline{1}\ 1]$ and loading axis, and the great circle representing planes in the $[1\ \overline{1}\ 1]$ zone axis. Under this definition, G1 has an χ angle $+22°$ and G2 $-29°$ Note that a positive χ always represents the MRSSP locates between a $\{110\}$ plane and a twinning $\{112\}_T$ plane while negative between a $\{110\}$ plane and an anti-twinning $\{112\}_{AT}$ plane. χ is in the range of $-30° \leq \chi \leq +30°$ due to the crystal symmetry.

Micropillars were prepared on single crystals and on the grain boundary between them by focused ion beam (FIB) with a gallium source on a dual-beam microscope (Tescan Lyra, Czech Republic). At an acceleration voltage of 30 kV, the pillars were brought into shape in a stepwise fashion starting from rough milling with a current of 5 nA, consecutive 1 nA and finally fine polishing at 200 pA. The milled micropillars have nominal diameters of 1 μm, 2 μm and 4 μm with an aspect ratio between 2~3. The exact dimensions for every pillar were measured on the same microscope before the compression testing.

The lamellae cross-section of selected deformed micropillars were lifted out by FIB with gallium source on a dual-beam microscope (Helios NanoLab 600i from FEI Inc). The acceleration voltage was set as 30 kV. Before lifting out, the micropillar top was protected with a 2μm platinum layer deposited by ion beam-induced deposition platinum with ion beam deposition to 2 μm thickness at 80 pA current. 21 nA followed by 2.5 nA was used to cut lamellae from targeted pillars. For shaping the lamella, currents of 0.79 nA and 0.23 nA were applied in sequence.

2.2. Micropillar compression

Micropillar compression tests were performed in a tungsten filament SEM (Zeiss DSM 962, Germany) equipped with an in-situ indenter system (Alemnis AG, Switzerland) in the cryogenic module, where liquid nitrogen in a 25 L dewar was evaporated on a fine copper grid and pumped through a cold finger attached to the indenter frame for cooling down both sample and indenter tip. Details of this setup can be found in [27]. A 10 μm diamond flat punch (Synthon MDP, Switzerland) was used for the tests. For the set of experiments concerning the size effect, the strain rate was 0.001 s^{-1}. For the strain rate effect, the testing strain rates were varied between 0.001 s^{-1}, 0.01 s^{-1} and 0.1 s^{-1}. For the temperature influence, tests at room temperature and −80 °C were performed at three strain rates (0.001 s^{-1}, 0.01 s^{-1} and 0.1 s^{-1}). The temperature −80 °C was the lowest we could reach on the sample surface with this setup, which lies slightly above the brittle to ductile transition temperature T_{DBT} (~ −100 °C for single electric steel with comparable composition [28]). However, both room temperature and −80 °C lie below the critical temperature T_c (~ 100 °C for single crystal [29]). At least three micropillars were tested at each condition. An overview of pillars tested at each condition is given in Table S1. The engineering stress was calculated by dividing the load by the top diameter of pillars and the engineering strain by dividing the

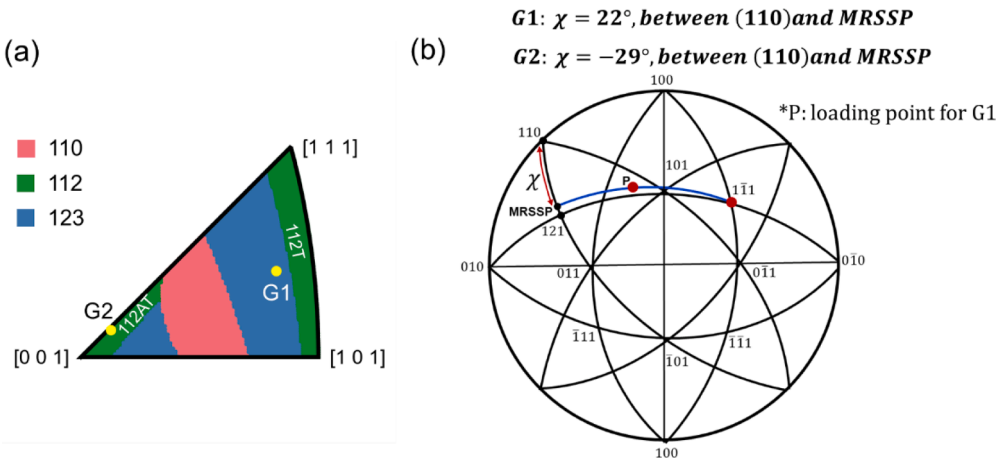

Fig. 1. (a) The orientation of the two crystals G1 and G2 shown in the IPF triangle. The colors divide the triangle into regions with slip plane families having the highest Schmid factor. (b) On the cubic stereogram, using G1 as an example, it shows the definition of χ angle between the MRSSP that contains the slip direction [1 $\bar{1}$ 1] and the neighbored [1 1 0] plane [25,26]. For G1, the χ angle is +22° and for G2 it is −29°.

displacement by the initial pillar height. The yield strength was determined at 0.5% engineering plastic strain, as graphically shown in Fig. S2.

2.3. Slip trace analysis

For slip trace identification, the deformed micropillars were imaged with a SEM (Mira, Tescan, Czech Republic) at two different views (frontside and backside). The activated slip system was identified by matching the actual slip trace(s) on SEM images of deformed pillars with the theoretical ones on a cylindrical model generated by Mathematica code, which uses the Bunge-Euler angles obtained from EBSD measurements [30]. To make a one-to-one comparison, an identical reference frame was aligned for imaging the pillars and acquiring EBSD maps. Furthermore, the cylindrical model was tilted to the same angle (45°) at which the image was taken and comparisons were made from front- and backside. An example is given in the supplementary materials (Fig. S3) to show the identification of slip traces. In this manuscript, slip traces marked with red color scheme represent activation of slip plane family {110}, green of {112}, and blue of {123}. Slip systems with the highest 15 Schmid factors are given in the supplementary materials in Table S2 in descending order.

2.4. Calculation of elastic anisotropy and stress incompatibility

As reported in [31], the elastic anisotropy of two crystals might influence slip system activation in bi-crystals. The elastic modulus along the loading direction, E_3, was calculated for each grain using its Euler angles and the elastic constants from [32] with a comparable Si content calculated based on density functional theory, which results in 225 GPa for G1 and 137 GPa for G2. The corresponding lateral Poisson's ratios are ν_{31}=0.517 and ν_{32}=0.074 for G1, and ν_{31}=0.375 and ν_{32}=0.375 for G2. Due to the large elastic anisotropy, the stress incompatibility was hence further calculated based on the methodology of Tiba et al. [31], with the elastic constants, Euler angles, grain boundary inclination angle and crystal volume fraction as input parameters. The calculation was implemented in Python and can estimate stress incompatibility in BCC, FCC, and HCP bi-crystals [33]. The resulting resolved shear stress values normalized by the macroscopic uniaxial stress $|\tau^s/\Sigma_u|$, predicted by Tiba's model and Schmid's law are compared in the supplementary table (Table S3).

3. Results

3.1. Influence of sample size

Before investigating the influence of the other two factors, namely, strain rate and temperature, we first focus on the sample size effect (at room temperature, and a strain rate of 0.001 s^{-1}) and aim to identify an appropriate pillar size for the following tests.

Fig. 2 shows the deformed micropillars of the two single grains with different diameters. Higher resolution images are given in Fig. S4. In G1 (single crystal grain 1), only one slip system is found and does not change with the tested sample size (Fig. 2a, d, g). It is consistently identified as (2 3 1)[1 $\bar{1}$ 1] with the highest Schmid factor ~0.49. By contrast, the sample size does influence the activation of slip systems in G2. For 1 μm pillars, whereas two out of three activate (1 2 $\bar{1}$)[$\bar{1}$ 1 1] (m~0.50 ranked #1) and ($\bar{1}$ 2 1)[1 1 $\bar{1}$] (m~0.41 ranked #14) (Fig. 2b), a pair of slip systems with relatively lower Schmid factor, specifically, (2 $\bar{3}$ 1)[1 1 1] (m~0.47, ranked #4) and (1 2 1)[1 $\bar{1}$ 1](m~0.46, ranked #7), is identified on the third pillar (Fig. 2c with slip trace labelled as *iii, iv*). Inconsistent slip activation is also found for 2 μm pillars, where two out of four activate (1 2 $\bar{1}$)[$\bar{1}$ 1 1] and ($\bar{1}$ 2 1)[1 1 $\bar{1}$] (Fig. 2e), and the other two activate (2 $\bar{3}$ 1)[1 1 1] and (1 2 1)[1 $\bar{1}$ 1] (Fig. 2f). However, for 4 μm pillars, they constantly activate the same pair of slip systems, (1 2 $\bar{1}$)[$\bar{1}$ 1 1] and ($\bar{1}$ 2 1)[1 1 $\bar{1}$], the former of which has the highest Schmid factor ~0.50. Overall, independent of pillar size, double-slip always occurs in G2 and single slip in G1.

In terms of bi-crystal compression, we note that the high angle grain boundary is transmittable, which is clearly visualized particularly for smaller pillars with 1 μm diameter, featured by continuous slip trace across the grain boundary (Fig. 3a_2, b_2). By analyzing the activated slip system in each grain, we can identify the slip transmission pair. As the slip traces on the bi-crystalline pillars are not as sharp and clear as on single crystalline ones, multiple theoretical traces with similarity are always presented on each grain side to highlight the matching. The matched one is given as a solid line. For each colored slip trace, their slip plane and slip directions are given in Fig. 3f.

For G1 in the bi-crystal, the activated slip system shows no difference at different pillar sizes, invariably (2 3 1)[1 $\bar{1}$ 1] (Fig. 3a_2, b_2, c_2, d_2, e_2), which is also the one identified in the single crystal. However, slip activation changes in the G2 part of the bicrystal. For 1 μm bi-crystalline pillars, G2 can activate either (2 3 $\bar{1}$)[$\bar{1}$ 1 1] or (1 1 0)[$\bar{1}$ 1 1] (Fig. 3a_1, b_1). The former has the second highest Schmid factor of 0.49 while the latter has the tenth highest of 0.43, neither of which is observed in single crystalline counterparts. These two slip systems are also found in 2 μm

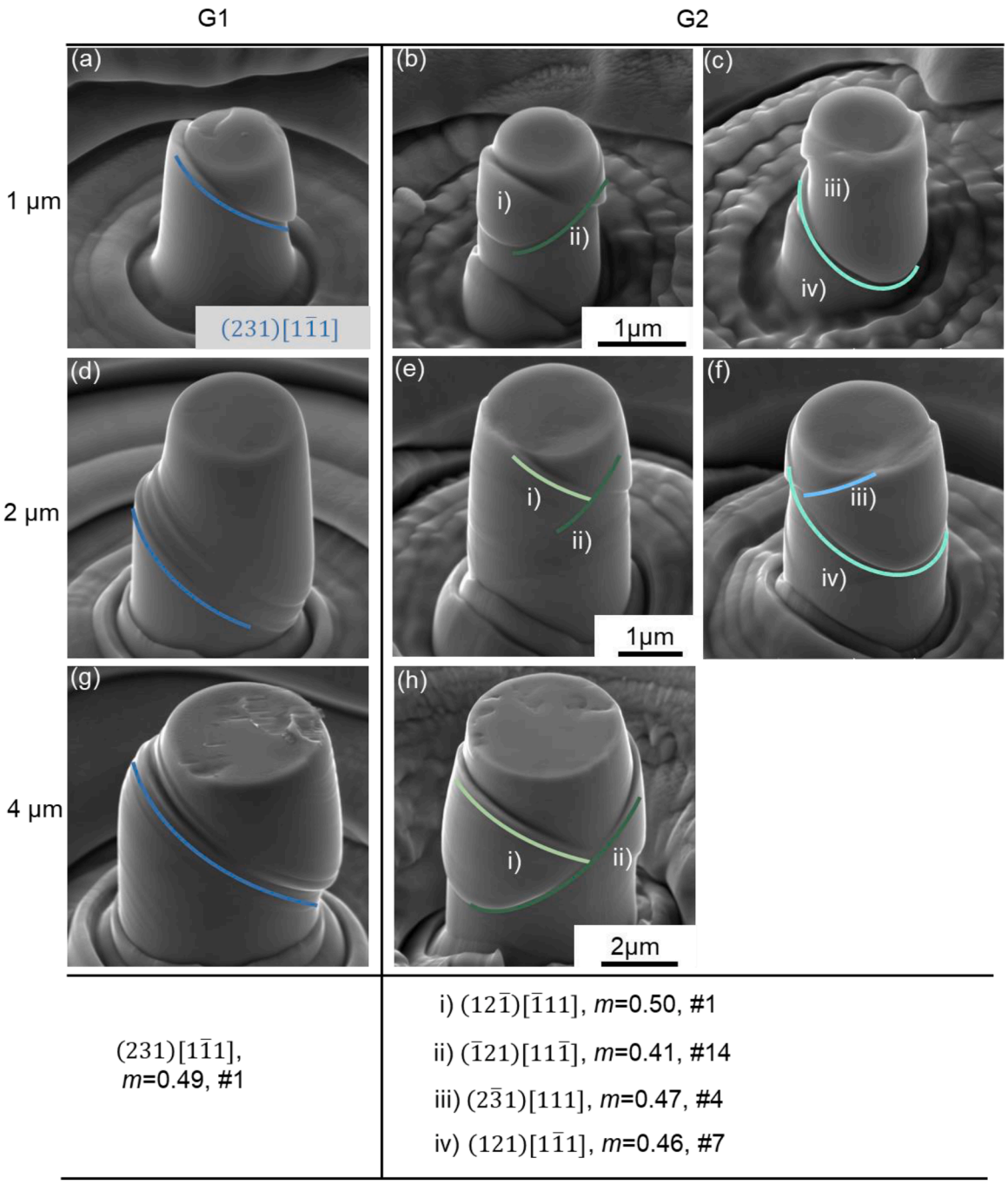

Fig. 2. Compressed micropillars of different diameters (1 μm, 2 μm, and 4 μm) with the identified activated slip systems (frontside). (a), (d) and (g) are from single crystal G1, with consistent activation of (2 3 1)[1 $\bar{1}$ 1], independent of pillar size. The other images are from G2, where two different micropillars are presented for 1 μm (b-c) and 2 μm (e-f) diameter to show different slip system activation. 4 μm pillars (h) always show a double-slip composed of (1 2 $\bar{1}$)[$\bar{1}$ 1 1] and ($\bar{1}$ 2 1)[1 1 $\bar{1}$]. For G2, differently colored slip traces are numbered, with corresponding slip system and Schmid factor listed below the images. Strain rate is 0.001 s^{-1} and temperature 25 °C.

bi-crystalline pillars (Fig. 3c_1, d_1). However, the 4 μm ones activate only (2 3 $\bar{1}$)[$\bar{1}$ 1 1] (Fig. 3e_1) without sign of (1 1 0)[$\bar{1}$ 1 1]. In addition to the identified slip systems, there are also vague and short slip traces near grain boundaries of smaller pillars (yellow lines in Fig. 3a_1, c_1), especially 1 μm ones, which are difficult to determine.

When only considering the sharp primary slip traces, the transmission factor m' equals 0.85 between (2 3 1)[1 $\bar{1}$ 1] in G1 and (2 3 $\bar{1}$)[$\bar{1}$ 1 1] in G2. When G2 activates (1 1 0)[$\bar{1}$ 1 1], the transmission factor is even higher, reaching 0.88.

Representative engineering stress-strain curves of micropillars with different diameters are given in Fig. 4a-c, showing a common "smaller is stronger" size effect at this scale range and accompanied by an increased number of load drops on the flow curves at a smaller size. Bi-crystalline pillars invariably yield at a higher stress and this stress difference is even more significant for 1 μm ones, consistent with the observation in [34]. Such increasing strength deviation between bi-crystalline and single crystals with decreasing pillar diameter is an implication of the characteristic length for dislocation source multiplication being the grain size instead of pillar diameter. For that, the size effect is described using grain size (determined by the half cross-section of bi-crystals) to fit all

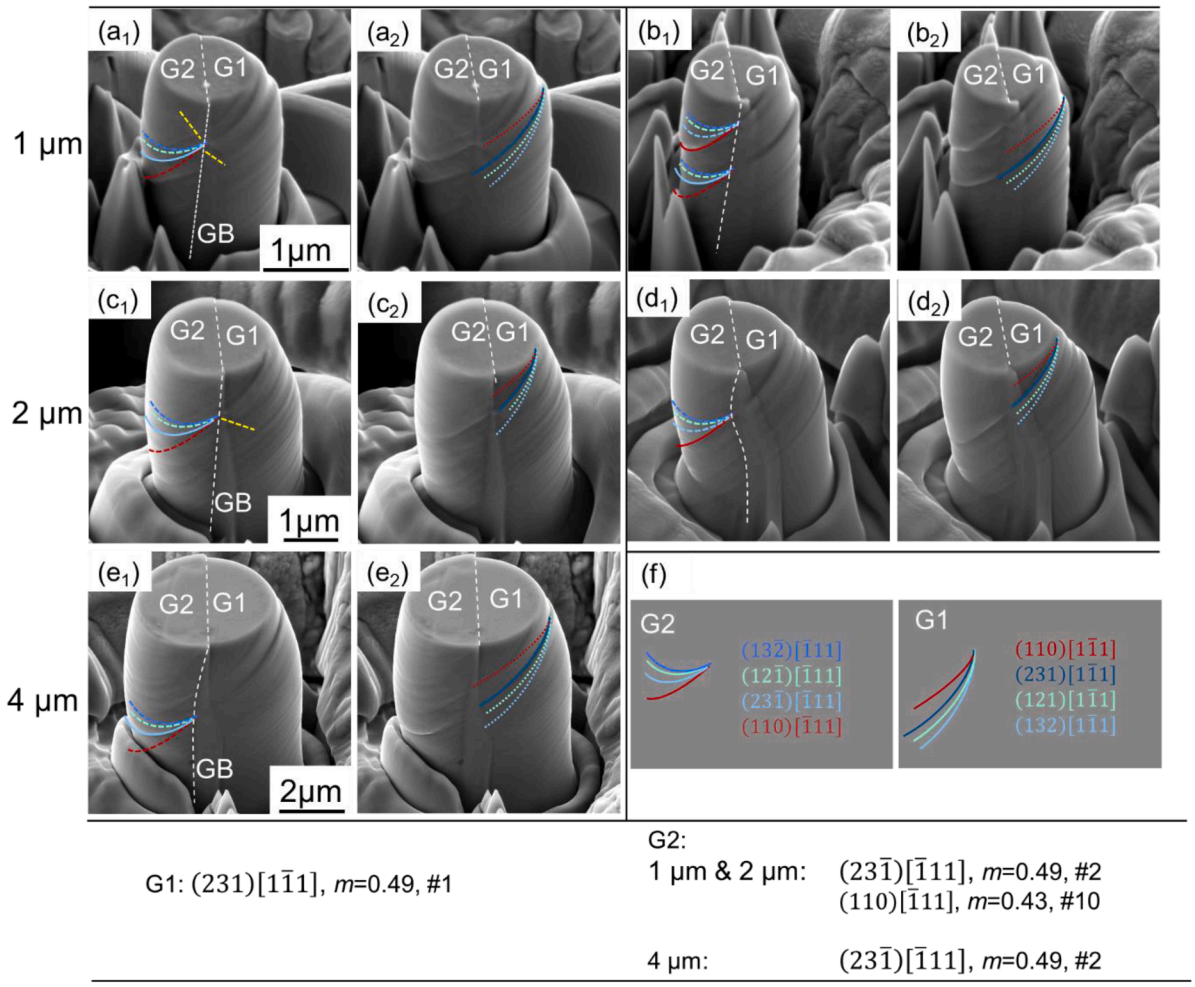

Fig. 3. Compressed bi-crystalline micropillars of different diameters (1 μm, 2 μm and 4 μm) with the identified activated slip systems (from backside). For 1 μm (a_1-b_2), and 2 μm (c_1-d_2) diameter, two different micropillars are presented to show different slip system activation. 4 μm (e_1-e_2) bi-crystalline pillars consistently show slip transmission between (2 3 1)[1 $\bar{1}$ 1] in G1 and (2 3 $\bar{1}$)[$\bar{1}$ 1 1] in G2. (f) gives the corresponding slip system of differently colored slip traces. Below the image list, the identified activated slip systems and their Schmid factor in G1 and G2 are listed. Strain rate is 0.001 s^{-1} and temperature 25 °C.

data points of G1, G2 and GB with a power law equation, as shown in Fig. 4d The fitting has a high R^2 value 0.985 and leads to a size scaling exponent of 0.42 (similar to our previous work ~0.37 [12]). Apart from the overall fit, the size effect of G1, G2 and GB is also separately described, with fitting results shown in Fig. S5. The size scaling exponents are 0.29, 0.46 and 0.55, respectively, being the smallest for G1 and comparable for G2 and GB. The origin of this orientation-dependent scaling behavior, however, remains unclear. At first glance, the G2 orientation, which favors multiple slip systems, may promote dislocation–dislocation interactions. Nevertheless, within the framework of the single-arm source model, enhanced elastic interactions are expected to reduce, rather than increase, the scaling exponent [35,36]. Alternatively, the larger exponent might be attributed to differences in lattice friction arising from the twinning–antitwinning asymmetry characteristic of bcc metals, as G2 lies in the antitwinning region (Fig. 1a). However, at room temperature, the effect of twinning–antitwinning asymmetry on lattice friction is expected to be negligible [30]. Furthermore, Schneider et al. reported the opposite trend, observing a smaller scaling exponent for the [001] antitwinning orientation in molybdenum [37]. Therefore, the physical origin of the orientation-dependent scaling exponent remains unresolved and requires further investigation. In any case, the scaling exponent lies in the reported range of 0.2 ~ 0.6 for BCC metals deformed at room temperature [38–40], which is lower than for FCC metals owing to the different contributions to the size-dependent yield strength, depending on homologous temperature, mobile dislocation density, and strain rate [41,42].

In addition to the size effect, the mechanical curves also reveal that bi-crystalline pillars constantly exhibit a high apparent strain hardening rate over different samples sizes, whereas the single crystalline counterparts are characterized by a weaker strain hardening with decreasing diameter. The constantly high strain hardening rate implies that the grain boundary, though transmittable, can effectively trap dislocations, which otherwise easily slip out in single crystal pillars, particularly those of small diameter.

3.2. *Influence of strain rate*

For the following section, we tested micropillars with a diameter of 4 μm to investigate the influence of strain rate (at room temperature) on slip system activation and mechanical properties. With this size, we can exclude the sample-size induced change in activated slip systems as shown in Fig. 2 and Fig. 3.

In the tested strain rate range, G1 constantly activates one slip system, which is identified as (2 3 1)[1 $\bar{1}$ 1] with the highest Schmid factor (Fig. 5a, b). The noticeable difference is that with increasing strain rate slip traces become less thick but more of them appear, which also applies to G2. In single crystal G2, apart from the frequently observed double-slip on (1 2 $\bar{1}$)[$\bar{1}$ 1 1] and ($\bar{1}$ 2 1)[1 1 $\bar{1}$] at 0.001 s^{-1} (Fig. 5c, g, slip

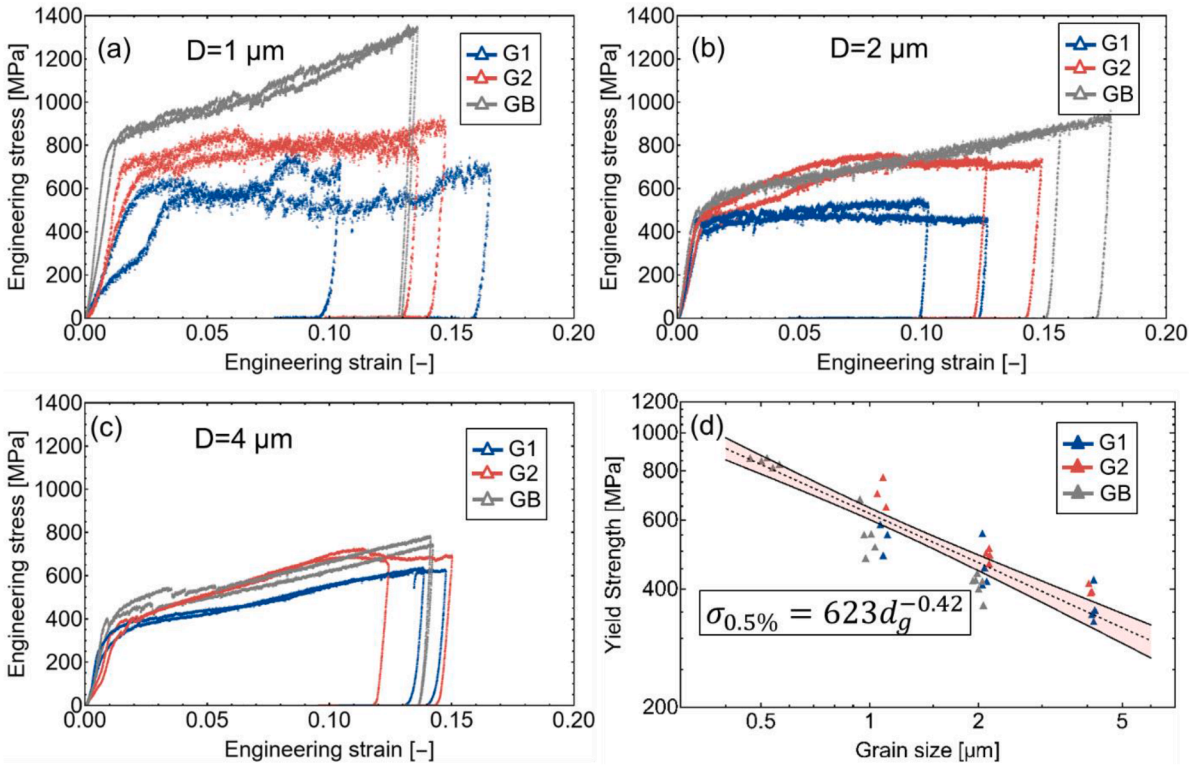

Fig. 4. Representative stress-strain curves of single crystalline and bi-crystalline pillars of different diameters in (a) 1 μm, (b) 2 μm, and (c) 4 μm. (d) Size effect fitted by a power law equation using grain size instead of pillar size. Strain rate is 0.001 s^{-1} and temperature 25 °C.

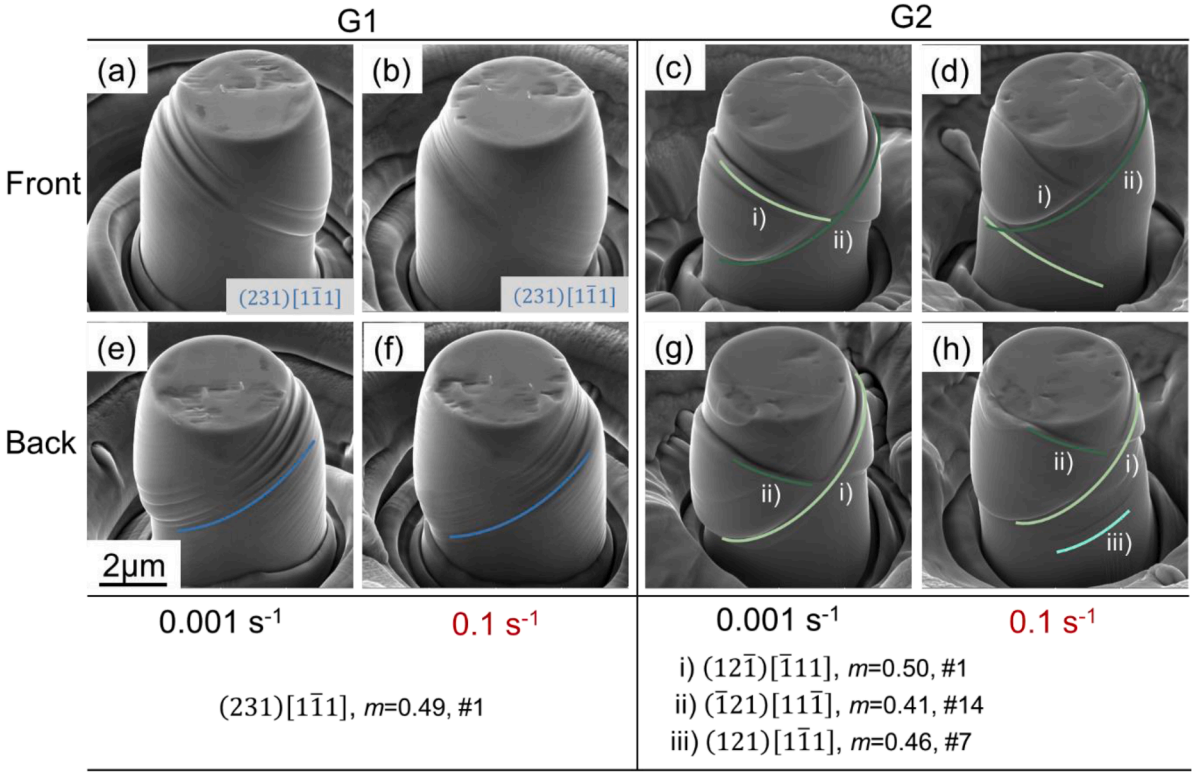

Fig. 5. Compressed single crystalline micropillars, tested at different strain rates (temperature at 25 °C and pillar size 4 μm) showing the identified activated slip systems from frontside and backside. (a, e) G1 tested at 0.001 s^{-1}. (b, f) G1 tested at 0.1 s^{-1}. (c, g) G2 tested at 0.001 s^{-1}. (d, h) G2 tested at 0.1 s^{-1}.

trace *i, ii*), a third slip system, (1 2 1)[1 $\bar{1}$ 1] with the seventh highest Schmid factor of 0.46, is also activated (Fig. 5h slip trace *iii*). This additional slip system is also activated in smaller pillars of 1 μm and 2 μm diameter (Fig. 2c, f). Higher resolution images are given in Fig. S6.

Within the tested range from 0.001 s^{-1} to 0.1 s^{-1}, strain rates do not change the slip transmission pair, which is identified as $(231)[1\ \bar{1}\ 1]$ for G1 with the highest Schmid factor (Fig. 6a_{II}, b_{II}) and $(23\bar{1})[\bar{1}11]$ for G2 with the second highest Schmid factor (Fig. 6a_I, b_I). Their transmission factor *m'* equals 0.85. Viewed from the opposite side (Fig. 6a_{III}, b_{III}), there are also faint slip traces in G2 possibly belonging to $(\bar{1}\ 2\ 1)[1\ 1\ \bar{1}]$ with a Schmid factor 0.41 present, which are observed in single crystalline G2. However, no visible slip transmission is associated with these traces, consistent with their very low transmission factor of 0.12 with $(231)[1\ \bar{1}\ 1]$ in G1.

Representative engineering stress-strain curves at different strain rates are given in Fig. 7a-b. When tested at 0.001 s^{-1}, bi-crystalline pillars begin to flow plastically at a slightly higher strength than the stronger single crystal G2. Specifically, taken at 0.5% plastic strain, the yield strength for the bi-crystal is 413 ± 26 MPa while it is 365 ± 41 MPa for G1 and 402 ± 12 MPa for G2. However, at 0.1 s^{-1}, the bi-crystal tends to yield at a comparable strength to that of G2 (453 ± 43 MPa for GB, 421 ± 24 MPa for G1 and 451 ± 22 MPa for G2). This change implies that the strain rate sensitivity (m_{SRS}) of single crystals and the bi-crystal can be different, which is calculated according to Eq. 2 [43]:

$$m_{SRS} = \frac{\partial \ln \sigma}{\partial \ln \dot{\varepsilon}} \tag{2}$$

Here, σ is the yield strength at 0.5% plastic strain and $\dot{\varepsilon}$ the applied strain rate, with results shown in Fig. 7c. In general, the bi-crystal has a slightly lower strain rate sensitivity than single crystalline counterparts, namely, 0.019 ± 0.009 for GB, 0.031 ± 0.015 for G1 and 0.025 ± 0.006 for G2. A comparison is made with the strain rate sensitivity of a polycrystalline Fe-Si alloy with a similar Si content to the alloy investigated in this work [44]. Within the error bars, given by twice the standard deviation of measurements for each condition, the strain rate sensitivity obtained here by micropillar compression is comparable to that by macroscopic tests.

3.3. Influence of temperature

We have compressed 4 μm micropillars at both room temperature (25 °C) and sub-ambient temperature (−80 °C). Although studying the effect of cryogenic temperatures on the deformation of 1 μm pillars would be of interest, particularly given their stronger dislocation–grain boundary interactions at room temperature, the increased noise generated by the nitrogen pump may cause fatigue-related artifacts owing to the substantially lower loads involved, as shown in Fig. S7.

The compressed single crystalline micropillars (at a strain rate of 0.1 s^{-1}) are shown in Fig. 8 with frontside and backside views. The activation of slip systems in G1 is not affected by the testing temperature and consistently identified as $(231)[1\ \bar{1}\ 1]$ with the highest Schmid factor 0.49 (Fig. 8a, b, e, f). By contrast, slip system activation is changed in G2. At room temperature, the identifiable slip traces *i* and *ii* (Fig. 8c, g) are $(1\ 2\ \bar{1})[\bar{1}\ 1\ 1]$ and $(\bar{1}21)[1\ 1\ \bar{1}]$. A third slip trace *iii* is found, possibly $(2\ \bar{3}\ 1)[1\ 1\ 1]$, as shown also in Fig. 5h. While these localized slip traces at room temperature are smooth, those at −80 °C are much wavier, as highlighted by yellow arrows on Fig. 8d, h. The waviness complicates the identification of activated slip systems. Following the average path of wavy slip traces, the most likely ones are labeled. The slip system $(1\ 2\ \bar{1})[\bar{1}\ 1\ 1]$ with the highest Schmid factor only exhibits faint traces and the second one $(\bar{1}21)[1\ 1\ \bar{1}]$ is suppressed at the low temperature.

Note that here the waviness comparison is only based on those localized slip steps. Apart from the localized slip traces used for slip system identification, there are also extremely fine and faint slip traces which are wavy in G2 at both temperatures, visible from high-resolution

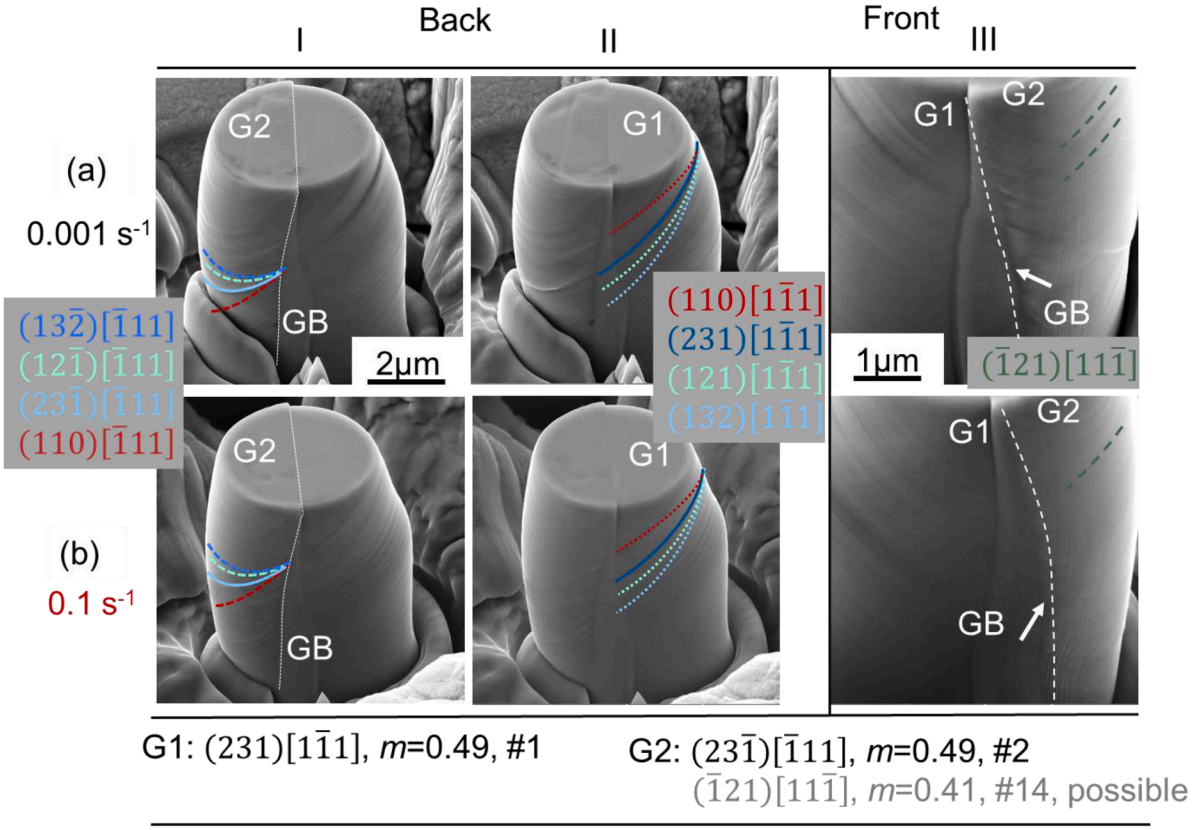

Fig. 6. Bi-crystalline micropillars compressed at different strain rates with the identified activated slip systems (temperature at 25 °C and pillar size 4 μm). The first row (a) at 0.001 s^{-1} and the second row 0.1 s^{-1}. Column I and Column II are backside view while Column III from frontside view at a higher magnification to show extra faint slip traces in G2. Slip transmission occurs between $(2\ 3\ 1)[1\ \bar{1}\ 1]$ in G1 and $(23\bar{1})[\bar{1}\ 11]$ in G2 at both strain rates.

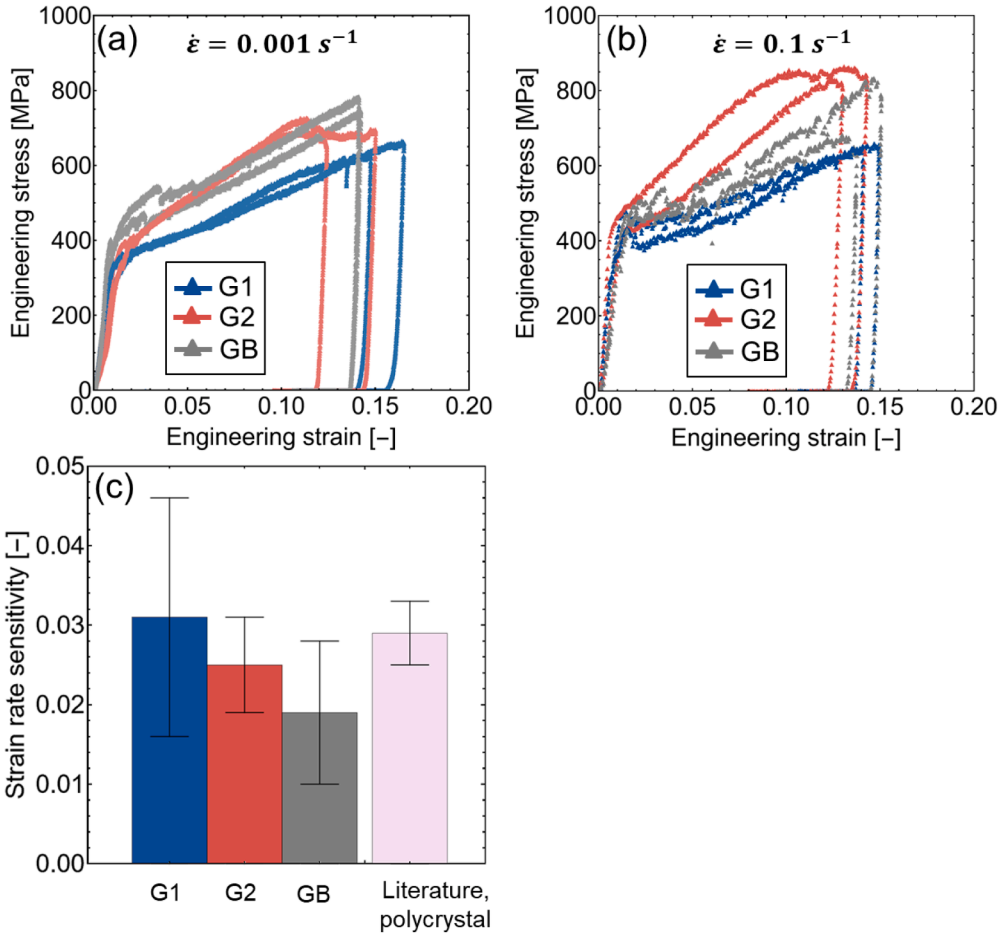

Fig. 7. Representative engineering stress-strain curves at a strain rate of (a) 0.001 s^{-1} and (b) 0.1 s^{-1}. (c) Strain rate sensitivity of single and bi-crystalline micropillars as well as polycrystalline bulk sample [44]. For the data shown here, the testing temperature is 25 °C and pillar diameter is 4 μm.

images (Fig. S4, Fig. S6 and Fig. S8).

In terms of bi-crystalline pillars, the low temperature of −80 °C does not change the transmission at the grain boundary and the transmission pair remains unaffected, specifically, $(231)[1\ \bar{1}\ 1]$ for G1 with Schmid factor $m = 0.49$ and $(23\bar{1})[\bar{1}\ 11]$ for G2 with $m = 0.49$ (Fig. 9a_I, a_{II} and Fig. 9b_I, b_{II}). Their transmission factor leads to $m' = 0.85$. The secondary slip traces (green and yellow dashed lines in Fig. 9a_{III}), resulting from dislocation activities on slip planes with a lower Schmid factor (most probably $(\bar{1}21)[1\ 1\ \bar{1}]$ in G2 and unknown in G1), disappear on the bi-crystalline pillars deformed at the lower temperature. Those wavy traces observed on single crystalline G2 pillars (Fig. 8d, h) are not found on bi-crystalline ones. After a comparable compressive strain (~ 13%), the grain boundary deformed at 25 °C shows a bulge while at −80 °C appears noticeably straighter (Fig. 9a_{III}, b_{III}). At a higher magnification, the yellow square inset (Fig. 9c) shows shear steps on the grain boundary deformed at −80 °C.

Representative engineering stress-strain curves at 25 °C and −80 °C are given in Fig. 10a, showing increased strength with decreasing temperature and also an upper yield point for bi-crystals (black arrow). Compared with data at room temperature, the occurrence of the upper yield point in bi-crystals leads to a noticeably instead of marginally higher yield strength (at 0.5% strain) than single crystals (731 ± 35 MPa for GB, 612 ± 5 MPa for G1 and 580 ± 33 MPa for G2), as shown in Fig. 10b However, this upper yield point related strength elevation disappears at larger strains (Fig. 10a). At −80 °C, we have also changed the testing strain rates, allowing a comparison of strain rate sensitivity at two temperatures (Fig. 10c). As a commonality for both single and bi-crystals, the strain rate sensitivity significantly increases with decreasing testing temperature, which aligns with literature for BCC materials [45]. Based on the yield strength at different strain rates, we can estimate the activation volume v^* by Eq. (3) [46], which is a commonly used indicator of the rate controlling mechanisms:

$$v^* = kT \cdot \frac{\partial \ln \dot{\varepsilon}}{\partial \sigma} \tag{3}$$

Here, k is the Boltzmann constant and T represents the testing temperature in Kelvin. The results are shown in Fig. 10d. At −80 °C, the activation volume for both single and bi-crystals is around 10 b^3, while at room temperature, the average value falls into the range of 35 ~ 49 b^3, where b is the Burgers vector of pure iron. The addition of 2.4 wt.% Si should have little influence on the lattice constant compared with pure iron [47]. The activation volume at both temperatures lies in the order of 10^1–10^2 b^3, which suggests the rate-limiting mechanism for dislocation motion is the Peierls barrier [48].

In order to have a better insight on slip activities at grain boundary and temperature influence, two deformed bi-crystalline micropillars (the two from Fig. 9) were selected for EBSD cross-sections. The results are shown in Fig. 11 with grain reference orientation deviation angle maps (with reference area outlined at the bottom of pillars). The bi-crystalline micropillar deformed at 25 °C exhibits a significantly higher misorientation angle than that deformed at −80 °C. The mean deviation angle is 3.91 ° at 25 °C while 2.53° at −80 °C. The 90th percentile at room temperature reaches ~ 12°, while approximately 6° for the lower temperature counterpart. Details are given as the cumulative curves in the Fig. S9. The wide distribution of deviation angles at 25 °C presents a strong localization region extending to grain boundary

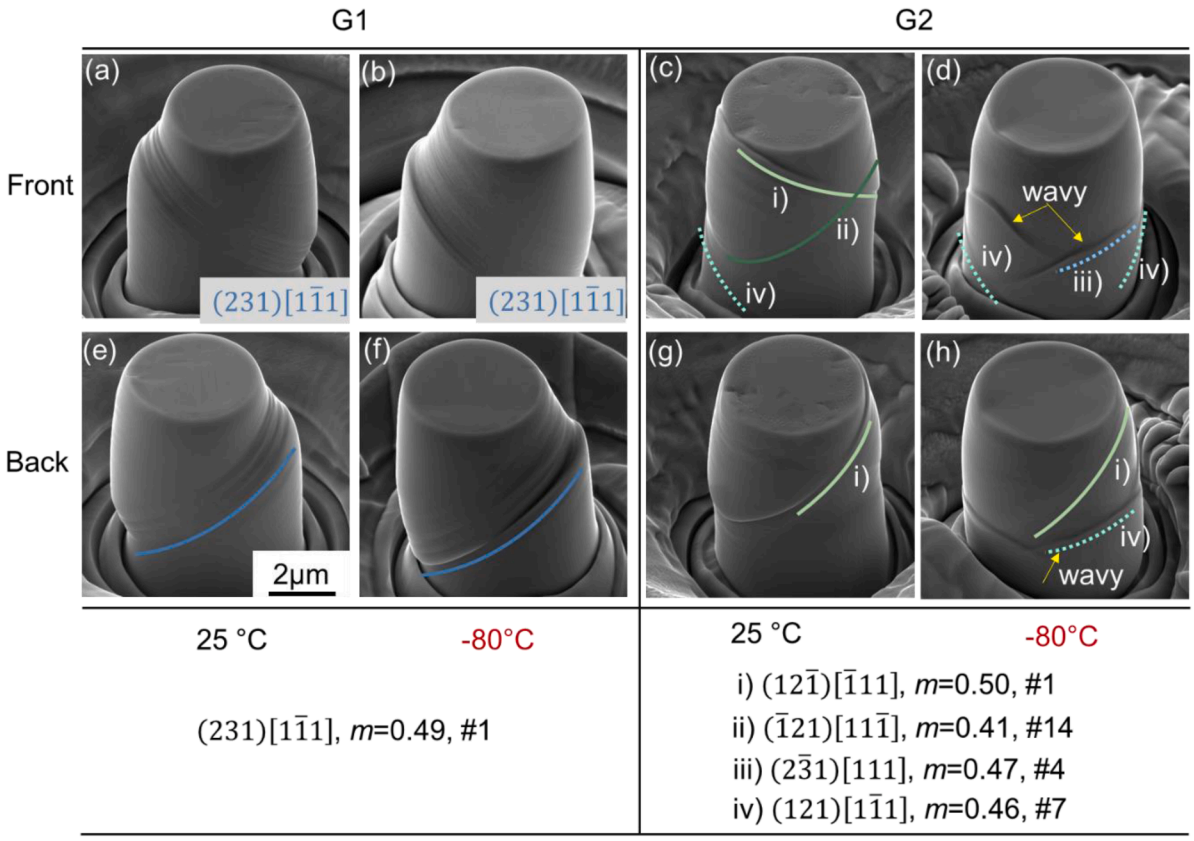

Fig. 8. Compressed single crystalline micropillars of 4 μm diameter tested at 25 °C and −80 °C (strain rate 0.1 s^{-1}), showing the identified activated slip systems. (a, e) and (b, f) are from single crystal G1 tested at 25 °C and −80 °C, respectively. (c, d) and (g, h) are from single crystal G2 tested at 25 °C and −80 °C, respectively. Frontside (a-d) and backside views (e-h) are provided.

that correlates with dislocation pileups at the grain boundary [49], which is not observed at the low temperature. This strong pileup inside the micropillar tested at room temperature can originate from the activation of secondary slip systems observed in both grains, as shown by dashed lines in Fig. $9a_{III}$, which are not favored for slip transmission and suppressed at the lower temperature. In other words, there are no significant dislocations pileups if only the transmission pair is involved in plastic deformation. The two images in Fig. $9a_{III}$ and Fig. $9b_{III}$ are provided in Fig. S10 for better visibility to show secondary slip traces near the curved grain boundaries. The strong pileups seem also inducing the grain boundary bulging as mentioned above, which can be an indication of grain boundary migration and requires further future investigation.

4. Discussion

4.1. Slip behavior in Fe-2.4 wt.% single crystals

In the investigated two single crystals, G1 consistently activates $(231)[1\ \bar{1}\ 1]$ with the highest Schmid factor, regardless of the testing conditions, specifically, the micropillar size, strain rate and temperature. In contrast, slip system activation of G2 is considerably influenced by these factors.

We first discuss the influence of micropillar size. At small length scales, dislocation sources are supposed to be limited and those lying on the slip plane with the maximum Schmid factor may not be favored to be activated, for instance, when the pinning point of the single arm dislocation sources is too close to the sample surface [50,51]. Hence, with decreasing pillar diameter, the probability to activate slip systems with lower Schmid factor increases, which explains the observation in G2 of slip activation on $(2\ \bar{3}\ 1)[1\ 1\ 1]$ with the fourth highest Schmid factor (double slip together with $(1\ 2\ 1)[1\ \bar{1}\ 1]$ (m~0.46, #7)). However, a question might arise, why does it tend to activate the one with the fourth highest Schmid factor in a different slip direction, instead of the colinear planes $(2\ 3\ \bar{1})[\bar{1}\ 1\ 1]$ and $(1\ 3\ \bar{2})[\bar{1}\ 1\ 1]$ with m ranked 2 and 3, respectively? This might be related to the small intersection angle between $(1\ 2\ \bar{1})[\bar{1}\ 1\ 1]$ with these two planes, namely only 11°. It implies that those unfavored dislocation sources (too close to surface) for slip system $(1\ 2\ \bar{1})[\bar{1}\ 1\ 1]$ with the highest Schmid factor would also be difficult to be activated on collinear neighboring {123} planes. Hence, it prefers activation of sources on slip planes with a different slip direction and simultaneously a high Schmid factor $(2\ \bar{3}\ 1)[1\ 1\ 1]$. This might also explain why in G1, the slip system does not change within the tested pillar diameter range. For G1, there are only 4 out of 48 slip systems with a Schmid factor higher than 0.4 (the first four collinear planes with slip direction $[1\ \bar{1}\ 1]$), while for G2, there are 16 out of 48. Hence, activating dislocation sources in G1 on slip planes with rather low Schmid factors might require even higher stress than activating unfavored sources on slip planes with high Schmid factors.

Upon increasing strain rate, according to the Orowan equation $\dot{\gamma} = \rho_m b v$, (with $\dot{\gamma}$ being the strain rate, ρ_m the mobile dislocation density, b the Burgers vector and v the average dislocation velocity), either more mobile dislocations or higher velocity are required to accommodate the externally applied strain. As suggested by the activation volume (Fig. 10d)), the rate controlling mechanism for dislocation motion in these 4 μm pillars is overcoming the Peierls barrier (v^* in the order of 10^1–10^2 b^3 [48]). While higher stress at higher strain rates reduces the energy barrier for dislocation motion and leads to a higher velocity, it can also promote the operation of sources that are initially unfavored or activation of slip systems with a lower Schmid factor. Consequently, we see more but faint slip traces (Fig. 5a, b) and also secondary slip system

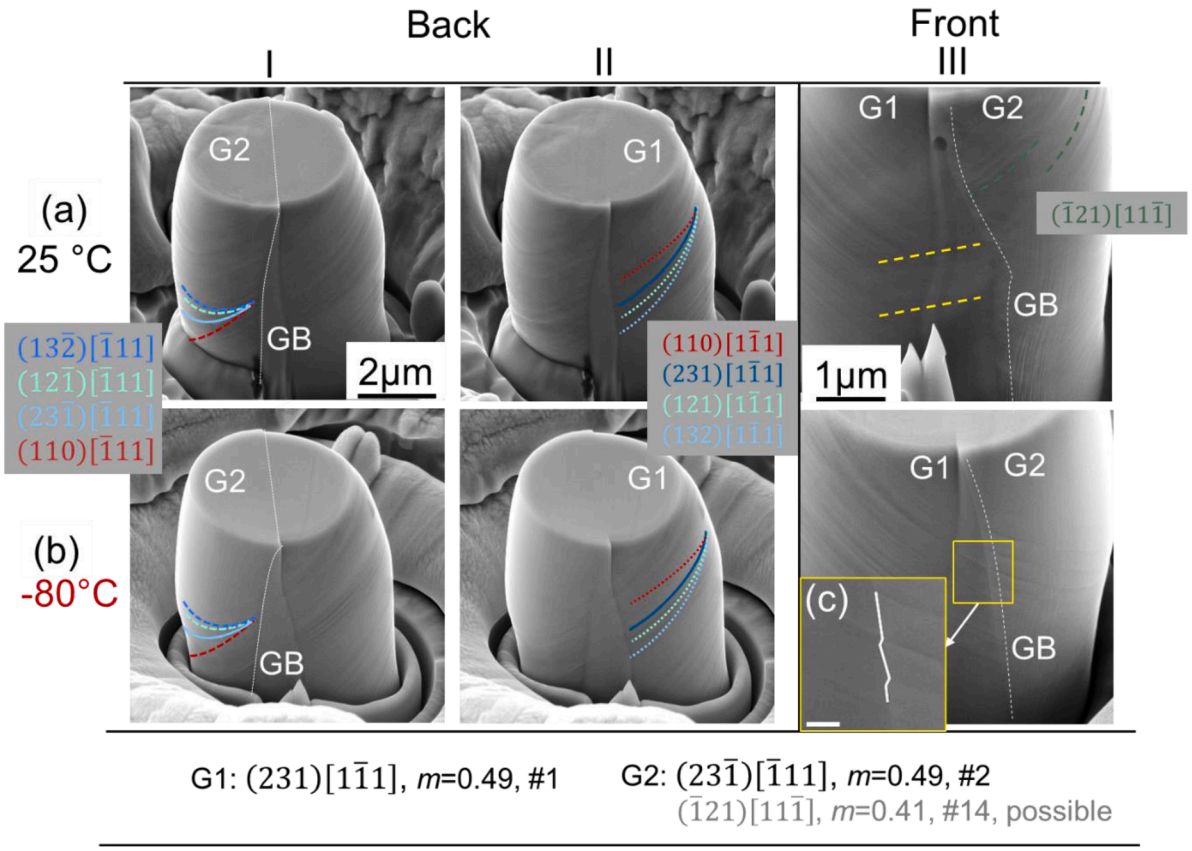

Fig. 9. Compressed bi-crystalline micropillars of 4 μm diameter tested at 25 °C and −80 °C (strain rate: 0.1 s^{-1}), showing the identified activated slip systems. The first row (a) at 25 °C and the second row at −80 °C. Column I and Column II are backside view, while Column III gives the frontside view at a higher magnification to show extra faint slip traces in G2 at 25 °C and more details at grain boundaries. Slip transmission occurs between (2 3 1)[1 $\bar{1}$ 1] in G1 and (23$\bar{1}$)[$\bar{1}$ 11] in G2 at both temperatures. The inset (c) shows the shear steps on the grain boundary deformed at -80 °C.

activation at higher strain rates (Fig. 5h).

Temperature has a significant influence on the activation of slip planes and the morphology of slip traces [21,52] and this influence is also orientation-dependent, as observed in our work. As shown in Fig. 1b, the loading axis of G2 leads to a positive Taylor angle $\chi = +29°$ in the anti-twinning direction under compression, whereas G1 exhibits a negative Taylor angle $\chi = -22°$ in the twinning direction. At room temperature, we observe the primary slip plane is (1 2 $\bar{1}$) in G2 and (231) in G1. In fact, for orientation G2, the angle between (110) and the observed activated slip plane (1 2 $\bar{1}$) is +30° and for orientation G1, the angle between (110) and the observed (231) is −19°, which implies that the observed slip planes are nearly the MRSSPs. Moreover, at room temperature, the CRSS on different slip plane families does not differ substantially [30,53,54]. This is also true in our case with $\tau_{\{123\}} \approx 206$ MPa (G1) and $\tau_{\{112\}} \approx 226$ MPa (G2). Hence, slip system activation is predominantly determined by the Schmid factor at room temperature. However, the observed localized {112} slip traces in G2 are probably only the apparent slip planes comprised of intensive cross slips between elementary {110} slip planes, as suggested by in-situ transmission electron microscopy tensile tests [55] and atomistic simulation [56]. The high-resolution images of compressed pillars in Fig. S4E,F,H, Fig. S6C, and Fig. S8C do show additional faint wavy slip traces apart from those localized thick slip steps on G2 deformed at room temperature. However, such relatively smooth localized slip traces can also become visibly wavy at lower temperatures. On one hand, cross slip is a thermally activated process [57]. Regular and frequent cross slips between elementary {110} slip planes to form an apparent slip can be hindered at lower temperature. The reduced thermal activation prolongs the duration of plasticity on one elementary slip plane and results in a longer straighter slip segment before crossing slip to another, which leads to much more pronounced signs of slip plane change (Fig. 8d). On the other hand, the temperature influence on the CRSS is orientation-dependent. The CRSS of the anti-twinning slip on {112} is more sensitive to the temperature [52,58–60] and increases noticeably more than that of {110}. The activation of {123} slip at sub-ambient temperatures in pure iron has not been frequently reported [54] and seems only to occur if {123} lies on the MRSSP, as in our case of G1. The CRSS of {123} at sub-ambient temperatures tends to fall between that of {110} and $\{112\}_{AT}$ in pure iron. By atomistic simulation, the CRSS of screw dislocation movement on {123} slip planes is even found comparable to that on {110} [61]. In either case, it remains lower than on $\{112\}_{AT}$. Hence, in single crystal G2, trajectory deviation from apparent $\{112\}_{AT}$ slip systems to {110} or {123} planes will be promoted at a lower temperature and constitute pronounced slip steps. Interestingly, in G1 consistently activating {123}, no obvious wavy features (neither localized nor faint traces) are observed at an identical magnification at either temperature, suggesting slip morphology is highly orientation-dependent. This smooth trajectory might result from two possibilities: first, the slip direction of {123} in G1 is easier forwarding [61] (see IPF in Fig. 1a), analogous to twinning direction of {112} slip system. Second, {123} itself can be an elementary slip, which requires further future study.

4.2. *Slip behavior in Fe-2.4 wt.% bi-crystal*

To discuss the slip behavior in the bi-crystal, we will focus on two aspects, specifically, slip transmission and mechanical properties of the bi-crystal.

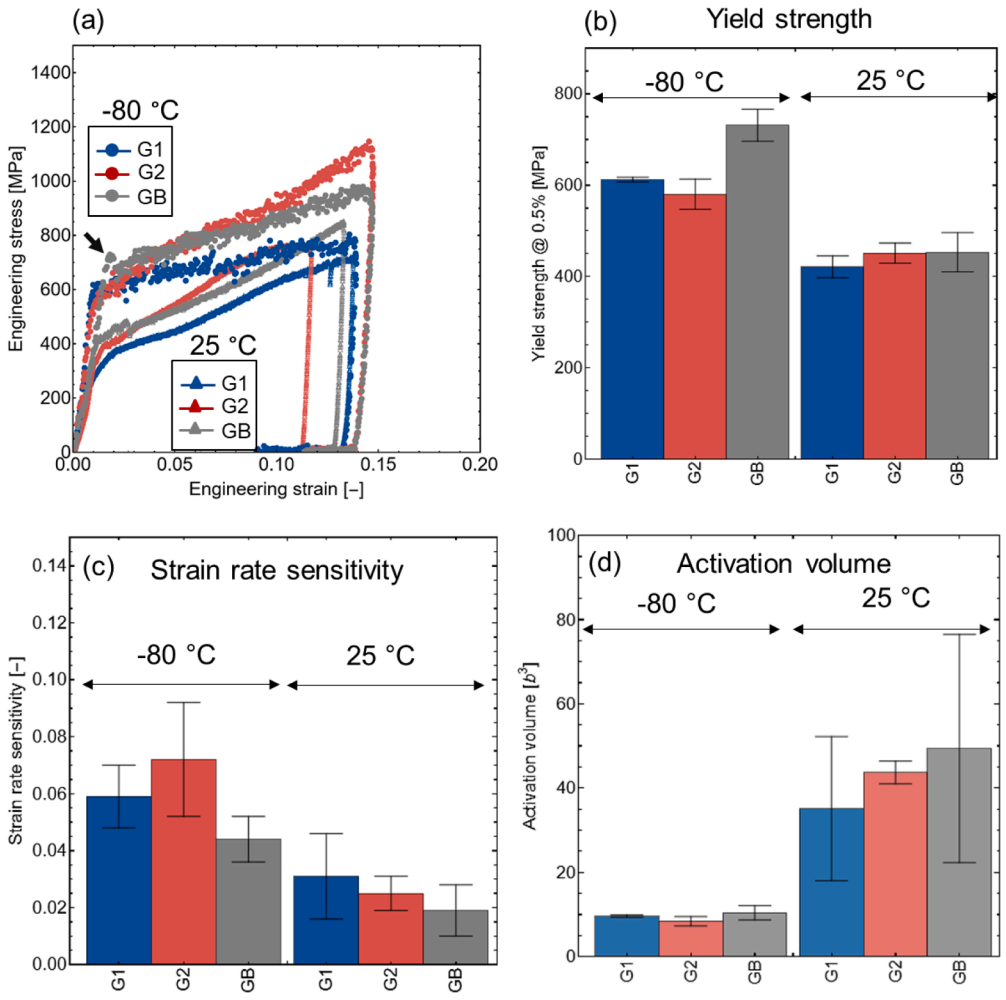

Fig. 10. (a) Representative engineering stress-strain curves at two temperatures. (b) Yield strength change with temperature. (c) Strain rate sensitivity and (d) activation volume at 25 °C and −80 °C. In (a) and (b), the strain rate is 0.1 s^{-1}. For all tests at −80 °C, pillar diameter is 4 μm.

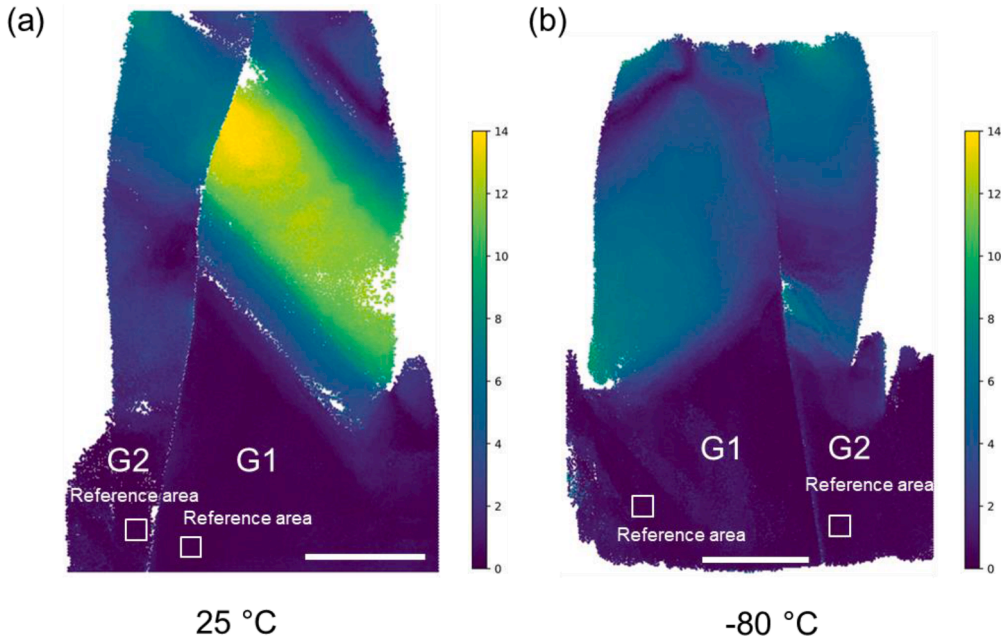

Fig. 11. Grain reference orientation deviation maps in degrees (°) of bi-crystalline pillar deformed at (a) 25 °C and (b) −80 °C. Strain rate: 0.1 s^{-1} and pillar diameter: 4 μm. The reference area for each grain is selected and outlined at the bottom of pillars. The scale bar for both (a) and (b) is 2 μm.

Whether a grain boundary is transmittable strongly depends on the transmission factor m' [23]. Based on literature, an m' factor > 0.8 indicates a favorable transmission event. For instance, slip transmission occurs in niobium grain boundaries, when $m' > 0.9$, independent of the grain boundary type [62]. For tantalum bi-crystals and polycrystals, slip transmission is observed when $m' > 0.85$ [16,63]. In a Ti-Al alloy, the threshold of this transmission factor stays around 0.78 [23], which is close to 0.76 for a copper high angle grain boundary [34].

In this work, regardless of the testing strain rate and temperature, we observe slip transmission between $(231)[1\ \bar{1}\ 1]$ (#1) in G1 and $(23\bar{1})[\bar{1}\ 11]$ (#2) in G2 for all 4 μm pillars, which have a transmission factor of 0.85 paired with high Schmid factors (both 0.49), making the transmission feasible and reasonable. However, another question might arise: why the bi-crystal does not activate transmission pair in a vise versa manner, namely, slip system with the highest Schmid factor in G2 and the one with the second highest in G1, which also have a high transmission factor ~ 0.86? This can be related with the incompatibility stress (provided in Table S3) arising from the pronounced difference in elastic response between the two grains, i.e., the elastic modulus along the loading direction (225 GPa for G1 and 137 GPa in G2) [31,32]. While Schmid's law predicts a comparable maximum shear stress in two grains, Tiba's model leads to a significantly higher maximum resolved shear stress in G1 (compare $|\tau^s/\Sigma_u|_{max}$=0.553 in G1 and 0.382 in G2). This difference implies that the plasticity onsets in G1, which needs to be further transmitted to G2. However, note that the incompatibility stress does not exert a great difference on the predicted shear stress order of slip systems in our case compared with that from Schmid's law (Table S3).

Noteworthy is that we did not observe wavy features in the G2 part of bi-crystalline pillars, when decreasing testing temperature, although waviness was observed in the G2 single crystals. This might be a result of the activation of $\{123\}$ planes instead of $\{112\}_{AT}$ in both grains, with the former supposedly having a lower CRSS than the latter at sub-ambient temperatures, as discussed for the slip in single crystals [52,54,58–61]. The predominantly identified $(1\ 2\ \bar{1})[\bar{1}\ 1\ 1]$ slip system with the highest Schmid factor in the G2 single crystal is not involved in transmission, in spite of its also relatively high $m' = 0.8$, which signifies the critical role of transmission factor in triggered slip planes for slip transmission. Once a sufficiently high Schmid factor is present, the transmission factor m' determines the transmission pair. For instance, Malyar et al. observed the slip transmission on a slip system with a Schmid factor of only 0.28, but with a transmission factor of 0.88 [34]. Although in the tested range, the strain rate and temperature do not influence slip systems involved in transmission, we do see an impact of micropillar size. For 1 μm and 2 μm pillars, transmission is also observed on $(1\ 1\ 0)[\bar{1}\ 1\ 1]$ and the involved slip system change can be similarly explained by source availability as discussed in the single crystal section (Section 4.1) [50]. It has the tenth highest Schmid factor of 0.43 and is not activated in the G2 single crystal. However, the transmission factor of this slip system reaches 0.88 with $(231)[1\ \bar{1}\ 1]$ in G1, which further suggests that the slip transmission factor plays a more dominant role than the Schmid factor.

The strength of a micropillar bi-crystal does, however, not have a direct relationship with any single slip transmission event or underlying transmission factor, rather, several parameters contribute to bi-crystal strength. Our results show that whether a bi-crystalline pillar with a transmitting grain boundary is stronger than or comparable with single crystals, depends on test parameters. While the bi-crystal is marginally stronger than single crystals (Fig. 4c) at a larger pillar size of 4 μm, 1 μm bi-crystalline pillars yield at a significantly higher strength (Fig. 4a). This size-dependent influence of a transmittable grain boundary on yield strength has been similarly reported in copper [34] and nickel [10,14], which is explained by an increased interaction between single-arm dislocation sources and grain boundaries at a smaller size. Therefore, the characteristic length scale for power-law fitting should be grain size rather than pillar size [34], leading to a decent fit of our data (Fig. 4d).

Apart from the micropillar size, strain rate also plays a role. As shown in Fig. 7c, the bi-crystal is less sensitive to strain rates and hence, even the marginal elevation in yield strength at 0.001 s^{-1} disappears at 0.1 s^{-1}. At even larger strain rates, this transmittable bi-crystal might have a lower yield strength than single crystals. Interestingly, such crossover induced by strain rates has also been observed in a transmittable bi-crystalline copper, but at a lower strain rate end (0.0001 s^{-1}) [15]. This is, because in the copper case, the bi-crystal has a higher strain rate sensitivity than single crystals. The strain rate sensitivity of a bi-crystal in fact matches the general picture well that in BCC metals, strain rate sensitivity decreases with reduced grain size (athermal contribution increases from Hall-Petch strengthening), and in FCC metals, vice versa (enhanced activities of grain boundaries)[43].

Last but not least, the low temperature tends to induce the occurrence of an upper yield point (only in bi-crystal) and results in a noticeably higher yield strength (at 0.5% small strain) of a bi-crystal compared with single crystals (Fig. 10b). Such instability of plasticity at grain boundaries is also reported as pop-ins by nanoindentation, which signifies the beginning of transmission events by pileup dislocations [7]. At room temperature, secondary slip systems that cannot transmit the grain boundary (see dashed slip traces in Fig. 9a_{III}) can also be activated and carry plasticity by dislocations multiplication (which later pile up in Fig. 11). However, at low temperatures only the transmittable slip pairs with high Schmid factor are activated due to a decreased mobile dislocation density [54,64]. Hence, the initiation of plasticity by breakthrough of incipient dislocations across a grain boundary will be more pronounced at low temperatures. Such difference could be proven by characterizing pillars before and after the appearance of the upper yield point, but this is beyond the scope of this work.

5. Conclusions

In this study, we have performed micropillar compression tests to investigate the influence of pillar size, strain rate and temperature on the deformation behavior of a Fe-2.4 wt.% Si bi-crystal with a high angle grain boundary as well as its paired single crystals. Based on the experimental results, the following conclusions can be drawn:

1. Slip system activation in single crystal can be influenced by micropillar size and strain rate, which has been associated with dislocation source availability and activation on the unfavorable slip planes.
2. Temperature can cause the transition of slip plane, from $\{112\}$ family at room temperature with highest Schmid factor, to $\{110\}$ family at sub-ambient temperature in spite of a lower Schmid factor. Such transition has been correlated with the different temperature sensitivity of critical resolved shear stress on respective slip plane family.
3. Slip transmission is observed in bi-crystals with a high transmission factor ($\geq$0.85) and simultaneously high Schmid factor. Transmission factor is more critical than Schmid factor to determine slip systems for transmission, which, can be different from that activated in single crystals.
4. We observe no influence of strain rate and temperature on the transmission pair in bi-crystals based on 4 μm pillars. However, a smaller pillar size at room temperature can induce transmission events between slip systems with a lower Schmid factor, but a higher transmission factor.
5. The size effect of the bi-crystal and single crystals can be well fitted together, if the grain size instead of pillar size is plotted, indicating the grain size is the characteristic length for source multiplication.
6. The strain rate sensitivity of the bi-crystal is lower than that of single crystals, which can lead to a crossover of their yield strength at larger strain rates. An upper yield point with decreasing temperature is observed in bi-crystal, signifying the beginning of slip transmission.

Declaration of generative AI and AI-assisted technologies in the writing process

During the preparation of this work the authors used the ChatGPT in order to improve language and readability as well as coding. After using this tool/service, the authors reviewed and edited the content as needed and take full responsibility for the content of the published article.

CRediT authorship contribution statement

Chunhua Tian: Writing – review & editing, Writing – original draft, Visualization, Methodology, Investigation, Formal analysis, Data curation, Conceptualization. **Hexin Wang:** Writing – review & editing, Investigation, Data curation. **Pei-Ling Sun:** Writing – review & editing, Investigation, Data curation. **Martina Freund:** Writing – review & editing, Investigation, Data curation. **Marcus Hans:** Writing – review & editing, Investigation, Data curation. **Maral Sarebanzadeh:** Writing – review & editing, Data curation. **Zhuocheng Xie:** Writing – review & editing, Data curation. **Gaurav Mohanty:** Investigation. **Jakob Schwiedrzik:** Methodology, Investigation. **Sandra Korte-Kerzel:** Writing – review & editing, Supervision, Project administration, Funding acquisition, Conceptualization.

Declaration of competing interest

The authors declare that they have no known competing financial interests or personal relationships that could have appeared to influence the work reported in this paper.

Acknowledgment

The authors acknowledge Dr. Maria Watroba for performing an EBSD map on the macroscopic sample, Dr. Martin Heller for providing the sample and Sang-Hyeok Lee for help with Python code. We appreciate the kind support of Dr. Thiebaud Richeton in terms of calculating stress incompatibility at grain boundary due to elastic anisotropy. S. Korte-Kerzel, Z. Xie, M. Hans, P.L. Sun and M. Freund gratefully acknowledge financial support by the Deutsche Forschungsgemeinschaft under the SFB1394 Structural and Chemical Atomic Complexity – From Defect Phase Diagrams to Material Properties, project ID 409476157.

Supplementary materials

Supplementary material associated with this article can be found, in the online version, at doi:10.1016/j.actamat.2026.122498.

Data availability

The data that support the findings of this study are available from the corresponding author upon reasonable request. The Python code calculating the stress incompatibility due to elastic anisotropy can be accessible through DOI: 10.5281/zenodo.20287564.

References

[1] A. Di Schino, J.M. Kenny, Grain refinement strengthening of a micro-crystalline high nitrogen austenitic stainless steel, Mater. Lett. 57 (12) (2003) 1830–1834.
[2] T. Huang, L. Shuai, A. Wakeel, G. Wu, N. Hansen, X. Huang, Strengthening mechanisms and Hall-Petch stress of ultrafine grained Al-0.3% Cu, Acta Mater. 156 (2018) 369–378.
[3] E. Hall, The deformation and ageing of mild steel: III discussion of results, in: Proceedings of the Physical Society Section B 64, 1951, pp. 747–753.
[4] A. Kunz, S. Pathak, J.R. Greer, Size effects in Al nanopillars: single crystalline vs. bicrystalline, Acta Mater. 59 (11) (2011) 4416–4424.
[5] M. Tschopp, D. McDowell, Grain boundary dislocation sources in nanocrystalline copper, Scr. Mater. 58 (4) (2008) 299–302.
[6] A. Ma, F. Roters, D. Raabe, On the consideration of interactions between dislocations and grain boundaries in crystal plasticity finite element modeling–theory, experiments, and simulations, Acta Mater. 54 (8) (2006) 2181–2194.
[7] W. Soer, K. Aifantis, J.T.M. De Hosson, Incipient plasticity during nanoindentation at grain boundaries in body-centered cubic metals, Acta Mater. 53 (17) (2005) 4665–4676.
[8] Y. Su, C. Zambaldi, D. Mercier, P. Eisenlohr, T.R. Bieler, M.A. Crimp, Quantifying deformation processes near grain boundaries in α titanium using nanoindentation and crystal plasticity modeling, Int. J. Plast. 86 (2016) 170–186.
[9] G. Dehm, B.N. Jaya, R. Raghavan, C. Kirchlechner, Overview on micro-and nanomechanical testing: new insights in interface plasticity and fracture at small length scales, Acta Mater. 142 (2018) 248–282.
[10] N. Kheradmand, H. Vehoff, Orientation gradients at boundaries in micron-sized bicrystals, Adv. Eng. Mater. 14 (3) (2012) 153–161.
[11] C.S. Kaira, S.S. Singh, A. Kirubanandham, N. Chawla, Microscale deformation behavior of bicrystal boundaries in pure tin (Sn) using micropillar compression, Acta Mater. 120 (2016) 56–67.
[12] M. Heller, J.-L. Gibson, R. Pei, S. Korte-Kerzel, Deformation of μm-and mm-sized Fe2. 4wt% Si single-and bi-crystals with a high angle grain boundary at room temperature, Acta Mater. 194 (2020) 452–463.
[13] P.J. Imrich, C. Kirchlechner, C. Motz, G. Dehm, Differences in deformation behavior of bicrystalline Cu micropillars containing a twin boundary or a large-angle grain boundary, Acta Mater. 73 (2014) 240–250.
[14] N. Kheradmand, H. Vehoff, A. Barnoush, An insight into the role of the grain boundary in plastic deformation by means of a bicrystalline pillar compression test and atomistic simulation, Acta Mater. 61 (19) (2013) 7454–7465.
[15] N. Malyar, G. Dehm, C. Kirchlechner, Strain rate dependence of the slip transfer through a penetrable high angle grain boundary in copper, Scr. Mater. 138 (2017) 88–91.
[16] J.S. Weaver, N. Li, N.A. Mara, D.R. Jones, H. Cho, C.A. Bronkhorst, S.J. Fensin, G. T. Gray III, Slip transmission of high angle grain boundaries in body-centered cubic metals: micropillar compression of pure Ta single and bi-crystals, Acta Mater. 156 (2018) 356–368.
[17] C.R. Weinberger, B.L. Boyce, C.C. Battaile, Slip planes in bcc transition metals, Int. Mater. Rev. 58 (5) (2013) 296–314.
[18] A. Keh, Work hardening and deformation sub-structure in iron single crystals deformed in tension at 298 K, Philos. Mag. 12 (115) (1965) 9–30.
[19] A. Opinsky, R. Smoluchowski, The crystallographic aspect of slip in body-centered cubic single crystals. II. Interpretation of experiments, J. Appl. Phys. 22 (12) (1951) 1488–1492.
[20] P. Franciosi, L. Le, G. Monnet, C. Kahloun, M.-H. Chavanne, Investigation of slip system activity in iron at room temperature by SEM and AFM in-situ tensile and compression tests of iron single crystals, Int. J. Plast. 65 (2015) 226–249.
[21] S. Takeuchi, T. Taoka, H. Yoshida, Orientation and temperature dependences of slip in single crystals of iron alloys, Trans. Iron Steel Inst. Jpn. 9 (2) (1969) 105–117.
[22] B. Šesták, J. Blahovec, The temperature dependence of slip planes in Fe-3.4% Si single crystals, Phys. Status Solidi. 40 (2) (1970) 599–607.
[23] J. Luster, M. Morris, Compatibility of deformation in two-phase Ti-Al alloys: dependence on microstructure and orientation relationships, Metall. Mater. Trans. A 26 (7) (1995) 1745–1756.
[24] Y. Oda, M. Kohno, A. Honda, Recent development of non-oriented electrical steel sheet for automobile electrical devices, J. Magn. Magn. Mater. 320 (20) (2008) 2430–2435.
[25] J. Christian, Some surprising features of the plastic deformation of body-centered cubic metals and alloys, Metall. Trans. A 14 (7) (1983) 1237–1256.
[26] C. Tian, G. Dehm, C. Kirchlechner, Influence of strain rate on the activation of {110},{112},{123} slip in ferrite of DP800, Materialia 15 (2021) 100983.
[27] J. Schwiedrzik, R. Ramachandramoorthy, T.E. Edwards, P. Schürch, D. Casari, M. J. Duarte, G. Mohanty, G. Dehm, X. Maeder, L. Philippe, Dynamic cryo-mechanical properties of additively manufactured nanocrystalline nickel 3D microarchitectures, Mater. Des. 220 (2022) 110836.
[28] K. Ha, C. Yang, J. Bao, Effect of dislocation density on the ductile-brittle transition in bulk Fe-3% Si single crystals, Scr. Metall. Mater. 30 (8) (1994).
[29] D. Stein, J. Low Jr, A. Seybolt, The mechanical properties of iron single crystals containing <5× 10− 3 ppm carbon, Acta Metall. 11 (11) (1963) 1253–1262.
[30] C. Tian, D. Ponge, L. Christiansen, C. Kirchlechner, On the mechanical heterogeneity in dual phase steel grades: activation of slip systems and deformation of martensite in DP800, Acta Mater. 183 (2020) 274–284.
[31] I. Tiba, T. Richeton, C. Motz, H. Vehoff, S. Berbenni, Incompatibility stresses at grain boundaries in Ni bicrystalline micropillars analyzed by an anisotropic model and slip activity, Acta Mater. 83 (2015) 227–238.
[32] T. Mohri, Y. Chen, M. Kohyama, S. Ogata, A. Saengdeejing, S.K. Bhattacharya, M. Wakeda, S. Shinzato, H. Kimizuka, Mechanical properties of Fe-rich Si alloy from Hamiltonian, NPJ. Comput. Mater. 3 (1) (2017) 10.
[33] Z. Xie, AnisoBicrystal_Schmid_Analyzer, Zenodo, 2026.
[34] N. Malyar, J.-S. Micha, G. Dehm, C. Kirchlechner, Size effect in bi-crystalline micropillars with a penetrable high angle grain boundary, Acta Mater. 129 (2017) 312–320.
[35] T.A. Parthasarathy, S.I. Rao, D.M. Dimiduk, M.D. Uchic, D.R. Trinkle, Contribution to size effect of yield strength from the stochastics of dislocation source lengths in finite samples, Scr. Mater. 56 (4) (2007) 313–316.
[36] R. Soler, J.M. Wheeler, H.-J. Chang, J. Segurado, J. Michler, J. Llorca, J.M. Molina-Aldareguia, Understanding size effects on the strength of single crystals through high-temperature micropillar compression, Acta Mater. 81 (2014) 50–57.

[37] A. Schneider, B. Clark, C. Frick, P. Gruber, E. Arzt, Effect of orientation and loading rate on compression behavior of small-scale Mo pillars, Mater. Sci. Eng. A 508 (1–2) (2009) 241–246.
[38] O.T. Abad, J.M. Wheeler, J. Michler, A.S. Schneider, E. Arzt, Temperature-dependent size effects on the strength of Ta and W micropillars, Acta Mater. 103 (2016) 483–494.
[39] S. Brinckmann, J.Y. Kim, J.R. Greer, Fundamental differences in mechanical behavior between two types of crystals<? Format?>at the nanoscale, Phys. Rev. Lett. 100 (15) (2008) 155502.
[40] A. Schneider, C. Frick, B. Clark, P. Gruber, E. Arzt, Influence of orientation on the size effect in bcc pillars with different critical temperatures, Mater. Sci. Eng. A 528 (3) (2011) 1540–1547.
[41] A. Schneider, C. Frick, E. Arzt, W. Clegg, S. Korte, Influence of test temperature on the size effect in molybdenum small-scale compression pillars, Philos. Mag. Lett. 93 (6) (2013) 331–338.
[42] S. Korte, W. Clegg, Discussion of the dependence of the effect of size on the yield stress in hard materials studied by microcompression of MgO, Philos. Mag. 91 (7–9) (2011) 1150–1162.
[43] Q. Wei, S. Cheng, K. Ramesh, E. Ma, Effect of nanocrystalline and ultrafine grain sizes on the strain rate sensitivity and activation volume: fcc versus bcc metals, Mater. Sci. Eng. A 381 (1–2) (2004) 71–79.
[44] B. Aronsson, L. Grånäs, Strain rate sensitivity and ductile-brittle behavior of polycrystalline Fe-Si alloys with 2.5, 3.5, and 4.5 wt pct Si, Metall. Trans. 2 (4) (1971) 1087–1093.
[45] V. Maier, A. Hohenwarter, R. Pippan, D. Kiener, Thermally activated deformation processes in body-centered cubic Cr–How microstructure influences strain-rate sensitivity, Scr. Mater. 106 (2015) 42–45.
[46] G. Gibbs, The thermodynamics of thermally-activated dislocation glide, Phys. Status Solidi. 10 (2) (1965) 507–512.
[47] M. Polcarová, S. Kadečková, J. Bradler, K. Godwod, J. Bąk-misiuk, Lattice parameters of Fe–Si alloy single crystals, Phys. Status Solidi. 106 (1) (1988) 17–23.
[48] H. Conrad, Thermally activated deformation of metals, JOM 16 (7) (1964) 582–588.
[49] S.S. Rui, L.S. Niu, H.J. Shi, S. Wei, C.C. Tasan, Diffraction-based misorientation mapping: a continuum mechanics description, J. Mech. Phys. Solids. 133 (2019) 103709.
[50] K. Ng, A. Ngan, Breakdown of Schmid's law in micropillars, Scr. Mater. 59 (7) (2008) 796–799.
[51] Y. Cui, P. Lin, Z. Liu, Z. Zhuang, Theoretical and numerical investigations of single arm dislocation source controlled plastic flow in FCC micropillars, Int. J. Plast. 55 (2014) 279–292.
[52] W. Spitzig, A. Keh, Orientation and temperature dependence of slip in iron single crystals, Metall. Trans. 1 (10) (1970) 2751–2757.
[53] C. Du, F. Maresca, M.G. Geers, J.P. Hoefnagels, Ferrite slip system activation investigated by uniaxial micro-tensile tests and simulations, Acta Mater. 146 (2018) 314–327.
[54] W. Spitzig, A. Keh, The effect of orientation and temperature on the plastic flow properties of iron single crystals, Acta Metall. 18 (6) (1970) 611–622.
[55] D. Caillard, Kinetics of dislocations in pure Fe. Part I. In situ straining experiments at room temperature, Acta Mater. 58 (9) (2010) 3493–3503.
[56] M. Gilbert, S. Queyreau, J. Marian, Stress and temperature dependence of screw dislocation mobility in α-Fe by molecular dynamics, Phys. Rev. B Condens. Matter. Mater. Phys. 84 (17) (2011) 174103.
[57] V. Vivekanandan, B. Anglin, A. El-Azab, A data driven approach for cross-slip modelling in continuum dislocation dynamics, Int. J. Plast. 164 (2023) 103597.
[58] A. Keh, Y. Nakada, Plasticity of iron single crystals, Can. J. Phys. 45 (2) (1967) 1101–1120.
[59] W. Spitzig, A. Keh, The role of internal and effective stresses in the plastic flow of iron single crystals, Metall. Trans. 1 (12) (1970) 3325–3331.
[60] D. Hull, Orientation and temperature dependence of plastic deformation processes in 3· 25% silicon iron, in: Proceedings of the Royal Society of London. Series A. Mathematical and Physical Sciences 274, 1963, pp. 5–20.
[61] X. Wang, S. Xu, W.-R. Jian, X.-G. Li, Y. Su, I.J. Beyerlein, Generalized stacking fault energies and Peierls stresses in refractory body-centered cubic metals from machine learning-based interatomic potentials, Comput. Mater. Sci. 192 (2021) 110364.
[62] M. Wang, A. Ngan, Indentation strain burst phenomenon induced by grain boundaries in niobium, J. Mater. Res. 19 (8) (2004) 2478–2486.
[63] T.R. Bieler, S.C. Sutton, B.E. Dunlap, Z.A. Keith, P. Eisenlohr, M.A. Crimp, B. L. Boyce, Grain boundary responses to heterogeneous deformation in tantalum polycrystals, JOM 66 (1) (2014) 121–128.
[64] F. Guiu, P. Pratt, The effect of orientation on the yielding and flow of molybdenum single crystals, Phys. Status Solidi. 15 (2) (1966) 539–552.